SCIENCE CHINA
Information Sciences

• RESEARCH PAPER •

June 2026, Vol. 69, Iss. 6, 162402:1–162402:11
https://doi.org/10.1007/s11432-025-4716-6

Electrostatically gated dissipation control in two-dimensional nanoelectromechanical resonators via strain-amplitude antagonism for record 928% Q tunability

Qinyuan JIANG[1†], Jiawei FANG[1†], Junfan CHEN[1], Menglin GUO[1,2], Ce ZHANG[1], Xinru ZHANG[1], Yongxi DING[1], You WANG[2], Haizhi SONG[2], Qiang ZHOU[1,3], Konstantin Yu. ARUTYUNOV[4,5], Guangcan GUO[1,6,7], Wenjie HOU[1*] & Guangwei DENG[1,3,6,7,8*]

[1]*Institute of Fundamental and Frontier Sciences, University of Electronic Science and Technology of China, Chengdu 610054, China*
[2]*South West Institute of Technical Physics, Chengdu 610041, China*
[3]*Key Laboratory of Quantum Physics and Photonic Quantum Information (University of Electronic Science and Technology of China), Ministry of Education, Chengdu 611731, China*
[4]*National Research University Higher School of Economics, Moscow 101000, Russia*
[5]*P.L. Kapitza Institute for Physical Problems RAS, Moscow 119334, Russia*
[6]*Laboratory of Quantum Information, University of Science and Technology of China, Hefei 230026, China*
[7]*Hefei National Laboratory, University of Science and Technology of China, Hefei 230088, China*
[8]*Institute of Electronics and Information Industry Technology of Kash, Kash 844000, China*

Received 21 July 2025/Revised 9 November 2025/Accepted 15 December 2025/Published online 8 May 2026

Abstract Resonators based on nanoelectromechanical systems (NEMS) using two-dimensional (2D) materials with high-quality factors and excellent electrical control are critical for tunable coherent phonon dynamics, resonant sensors and wireless communications. However, their performance is fundamentally limited by the lack of a unified framework governing energy dissipation mechanisms and their electrical tunability. Here, we synergistically modulate both static tensile strain (ε) and dynamic vibration amplitude (δz) through electrostatic gating, achieving deterministic control over thermoelastic dissipation pathways in 2D doubly-clamped resonators. By combining analytical modeling with experimental measurements on MoS_2 and graphene devices, we demonstrate that ε suppresses dissipation, while δz amplifies dissipation. The interaction of these effects can control the dependence of Q on DC gate voltage V_G, including the non-monotonic trend and the record-breaking tunability range of $\Delta Q/Q = 928\%$. Crucially, we identify a critical regime where the strain-to-amplitude sensitivity ratio $(\partial\varepsilon/\partial V_G)/(\partial\delta z/\partial V_G)$ governs the Q-V_G relationship polarity, resolving long-standing discrepancies in literature. This universal framework demonstrates that through the control of initial strain and vibration amplitude, it is feasible to achieve the desired modulation of Q, thus paving the way for 2D NEMS applications in topological phononic circuits, quantum-limited mass sensing, and adaptive on-chip signal processing.

Keywords 2D NEMS, quality factor, strain tuning, MoS_2 resonators, graphene resonators

Citation Jiang Q Y, Fang J W, Chen J F, et al. Electrostatically gated dissipation control in two-dimensional nanoelectromechanical resonators via strain-amplitude antagonism for record 928% Q tunability. Sci China Inf Sci, 2026, 69(6): 162402, https://doi.org/10.1007/s11432-025-4716-6

1 Introduction

Nanoelectromechanical systems (NEMS) offer unique opportunities for probing the operating characteristics and properties of mechanical devices at the sub-micrometer scale [1–3]. An increased oscillation frequency [4] enables high sensitivity for detecting forces and masses [5–8], as well as to characterize properties at ultra-low temperatures, where quantum limits become significant [9–12]. Furthermore, in the 21st century, two-dimensional (2D) materials [13, 14] like graphene, molybdenum disulfide (MoS_2) have demonstrated a range of unique structural, mechanical, electrical, and optical properties [15, 16] distinct from those of traditional three-dimensional materials. This is largely due to their unique interlayer van der Waals interactions and various quantum confinement effects [17]. Characteristics of 2D materials include atomic-level thickness, flexibility, high mobility, and novel phenomena like

* Corresponding author (email: wjhou@uestc.edu.cn, gwdeng@uestc.edu.cn)
† These authors contributed equally to this work.

superconductivity [18], valley spin effect [19], quantum Hall effect [20], and 2D excitons [21, 22], among others. NEMS resonators constructed from 2D materials offer notable advantages over alternative resonators [23–26]. Their ultra-thin structure, characterized by high elastic modulus and low mass density, enables the development of ultra-high frequency resonators [27, 28]. Additionally, the atomic-layer thickness of 2D materials increases the effective area, which is crucial for the sensitive detection of mass, force, and pressure [29–31]. Finally, 2D resonators possess a wider linear dynamic range and remarkable inherent flexibility, allowing for high-frequency tunable and coupled resonators [32].

The quality factor (Q), which characterizes the energy decay rate in each vibration cycle, is the most critical parameter of an NEMS resonator. It is common to define all the dissipation of the resonator as the inverse of Q (Q^{-1}). The one with a higher Q accumulates more energy in a specific vibrational mode before dissipating it into the environment [33]. This property closely relates to the noise associated with thermomechanical displacement, which is essential for designing high signal-to-noise ratio sensors [34,35], low-phase-noise oscillators, and filters with substantial noise rejection. Consequently, high-Q resonators find application in precision measurements, including biosensors [36], inertial sensors [37], gas sensors [38], mass sensors [39], electromechanical signal processing [40], as well as frequency synthesizers [41] for wireless transmission and parametric amplification [42].

However, conventional resonators possess a fixed Q, imposing a static trade-off between competing performance metrics: a high Q enables fine frequency selectivity and low phase noise at the expense of bandwidth and response speed, while a low Q favors rapid transient response ($\tau \approx \frac{2Q}{\omega_0}$) and wideband operation but compromises resolution and sensitivity [43,44]. This fundamental compromise limits the versatility of individual devices in systems demanding dynamic adaptability, such as cognitive radios [45] that switch between narrowband and wideband protocols, or sensors that alternate between high-precision measurement and fast tracking modes. Overcoming this limitation requires resonators with freely electrically tunable Q, a capability that remains elusive.

Despite their exceptional potential, the performance of 2D NEMS resonators is fundamentally constrained by energy dissipation mechanisms that degrade their quality factor (Q). While NEMS devices inherently operate at higher frequencies than conventional MEMS counterparts, their Q-values remain significantly lower under comparable conditions [46], primarily due to unresolved intrinsic dissipation pathways. Extrinsic dissipation sources, such as air damping and structural losses, have been mitigated through vacuum operation and geometric optimization [4]. However, intrinsic mechanisms—including surface defects, thermoelastic damping, and phonon scattering—persist as dominant limitations, particularly in atomically thin 2D materials where high surface-to-volume ratios exacerbate surface losses. Recent studies on silicon nitride resonators suggest tensile strain engineering as a promising route to suppress thermoelastic dissipation [47], yet its applicability to 2D NEMS remains unexplored.

Our work addresses this critical gap by establishing a dual-strain modulation paradigm that modulates both static tensile strain (ε) and dynamic vibration amplitude (δz) through electrostatic gating. Contrary to prior observations in low-strain MoS_2 resonators (where Q increases with an increase in DC voltage) [48], we reveal a counterintuitive regime: devices with high initial strain demonstrate a decrease in Q with an increase in DC voltage. Systematic analysis identifies the strain-to-amplitude sensitivity ratio $(\partial\varepsilon/\partial V_G)/(\partial\delta z/\partial V_G)$ as the governing parameter for Q-V_G relationship polarity. This framework resolves long-standing discrepancies in literature, achieving a record Q tunability ($\Delta Q/Q = 928\%$) through synergistic control of ε and δz. Validated across MoS_2 and graphene resonators, our results demonstrate universal scaling laws: ε suppresses dissipation, while δz amplifies dissipation. These insights redefine strategies for optimizing 2D NEMS in quantum sensing and adaptive signal processing.

2 Materials and methods

To explore the relationship between Q and V_G, a range of doubly-clamped NEMS resonators has been devised. The substrate features multiple contact electrodes (source-drain electrodes) and gate electrode trenches arranged in series, utilizing a local-gate device structure design that facilitates large-scale integration while minimizing parasitic capacitance. Subsequently, appropriate strips of 2D material are transferred onto the electrodes. These materials are clamped by the source (S) and drain (D) electrodes, thereby forming multiple independent resonators (Figure 1(a)). The gate (G) at the bottom is used for electric excitation. With the source grounded, the DC signal V_G is provided by the DC voltage source and the AC signal δV_G is fed from the built-in generator of the Zurich UHFLI lock-in amplifier. Both DC and AC signals are simultaneously applied to the gate (G) using the Bias-Tee to drive the resonator. Concurrently, measurements are conducted using laser interference (LGK 7665-18, LASOS), whereby the reflected signal is directed back to the lock-in amplifier through a photodetector (FPD510-FS-VIS, Menlosystems) (Figure A1). By monitoring the lock-in amplifier output, the drive voltage is adjusted to maintain a stable resonance condition within the linear range. The samples are located inside a vacuum chamber at a temperature of

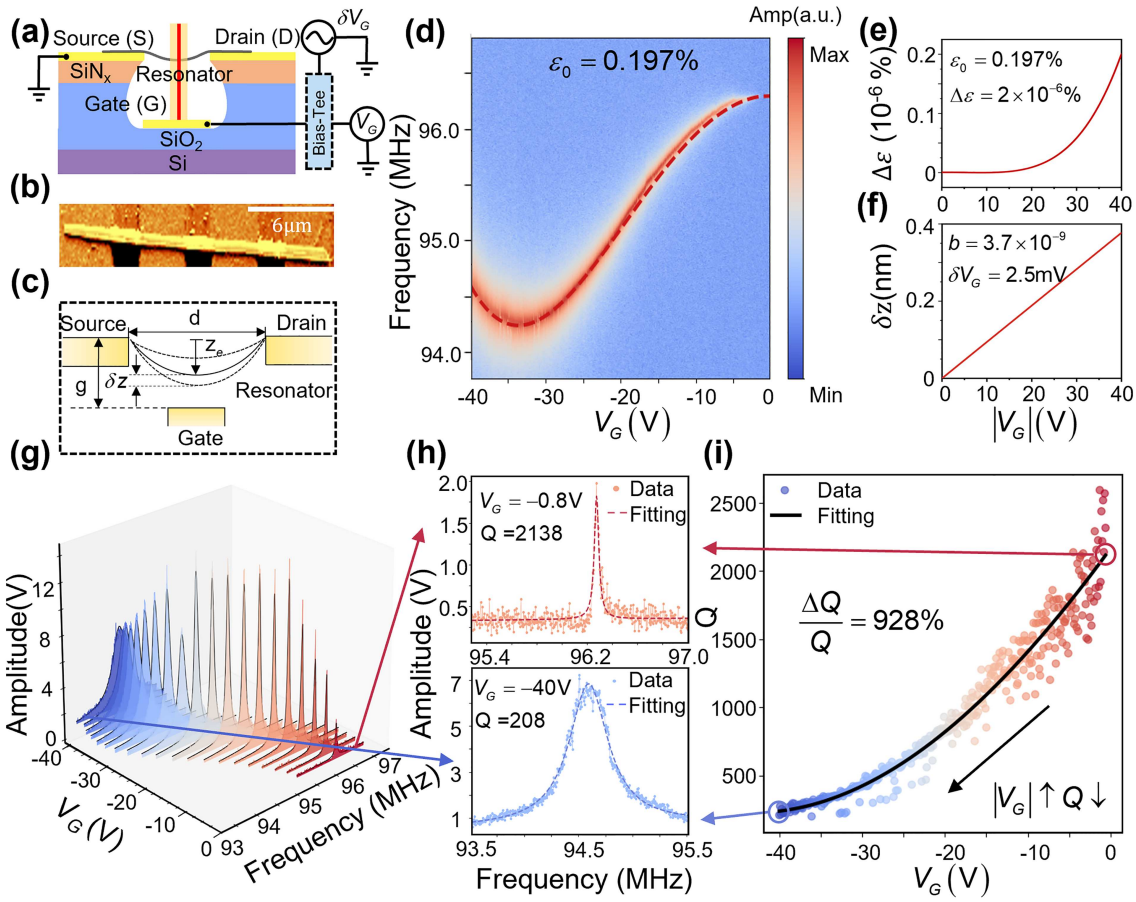

Figure 1 (Color online) Schematic diagram and resonance measurements of the doubly clamped resonator, and the dependence of Q on V_G for the resonator. (a) Schematic cross-section of the doubly clamped resonator V_G. The AC voltage δV_G from the lock-in amplifier and the DC voltage V_G from the DC voltage source are applied to the gate in order to drive the resonator and adjust its frequencies. The device operates in a vacuum chamber equipped with a quartz window. (b) An atomic force microscopy (AFM) image of a doubly-clamped MoS_2 resonator with length $L = 1.3$ μm, width $w = 1.9$ μm, and thickness $t = 50$ nm. (c) Schematic of the resonator device. In the doubly-clamped configuration, the uniform electrostatic force results in static deflection towards the gate. This equilibrium point can be denoted as z_e, the dynamic range (equal to vibration amplitude) as δz, and the distance between the gate and the contact electrode as g. (d)–(f) Measurements and theoretical analysis of the doubly-clamped MoS_2 resonator in (b) are conducted. (d) Various resonance spectra were measured at a constant AC drive amplitude of 2.5 mV, with the signal amplitude depicted on a color scale. The red dashed line represents the fit to the resonance, from which the initial strain of about 0.197% is derived. (e) Calculation of the total strain as a function of V_G. (f) A plot of the vibration amplitude versus V_G for a constant AC drive amplitude of 2.5 mV and the vibration amplitude coefficient b, computed from the geometry of the measured device in (b) and the device parameters. (g) 3D plot of the resonance spectrum measured in the range from 0 to −40 V. (h) Resonance spectra were taken at −0.8 V (top panel) and −40.0 V (bottom panel), leading to $Q = 2138$ and $Q = 208$, respectively, resulting in $\Delta Q/Q = 928\%$. The dashed lines depict the experimental data, while the dotted lines show the model fits. (i) Q-factors were obtained in the range from 0 to −40 V for the fundamental bending mode. The dots display the scattered experimental data, with the solid black line representing the model fit. Nonlinear resonance data have been excluded from this illustration for clarity.

about 6 K.

Figure 1(c) illustrates the voltage-driven schematic of the resonator. As the DC gate voltage V_G increases gradually, the strip is pulled down due to the electrostatic force, resulting in elongation and the subsequent generation of DC tensile strain. At this point, the distance of the strip from its initial position, i.e., the static tensile displacement, is denoted as z_e. When the AC drive signal δV_G is applied onto the gate, the levitated strip undergoes periodic forced oscillations at the round position z_e with the frequency of the drive signal adjusted being equal to the strip eigenfrequency. The vibration amplitude is denoted as δz. The vacuum gap between the strip and the gate will change periodically, resulting in a change of reflectivity, which is then used to obtain the reflection spectrum.

3 Results and discussion

In this case study, we examine a doubly-clamped MoS_2 NEMS resonator, characterized by a strip measuring 1.3 μm in length, 1.9 μm in width, and 50 nm thick, freely suspended on SiN_x with an initial air gap (g) of about 200 nm.

The atomic force microscopy (AFM) diagram for this configuration is presented in Figure 1(b).

It is worth noting that although the width-to-length ratio of this device is closer to that of a diaphragm, its boundary conditions—clamped only at the two electrode ends—conform to a doubly-clamped strip configuration. All experimental data presented here, unless otherwise specified, correspond to the fundamental vibration mode, in which both strip and diaphragm structures exhibit equivalent vibrational behavior with uniaxial strain dominance along the longitudinal direction (see Appendix D.3 for details). Therefore, the subsequent analysis appropriately follows the strip (beam) theory.

When V_G is applied, the total static strain in the MoS_2 strip consists of both the initial and the electrostatic V_G-induced tensile strains, which can be extracted from the measured resonance frequency tuning spectra. As shown in Figure 1(d), in case of the doubly-clamped MoS_2 strip resonator mentioned, 0.197% of the initial strain was extracted through data fitting the resonance frequency versus $|V_G|$ curve as V_G is scanned from -40 to 0 V (see Appendix B.2 for details). It should be noted that the initial strain ε_0 will vary between devices due to the particular intrinsic properties of the sample and the transfer techniques employed. The dissipation mechanism in MoS_2 NEMS resonators is primarily determined by two factors: the initial strain (ε_0), which is the built-in tension, and the induced tension due to stretching caused by V_G.

Q-factor of a resonator is defined as the ratio:

$$Q = 2\pi \frac{W_{\text{stored}}}{W_{\text{dissipated}}}, \tag{1}$$

where W_{stored} is the energy stored in the resonator and $W_{\text{dissipated}}$ is the energy dissipated per cycle. Several types of dissipation-induced losses affect Q in NEMS resonators, such as gas friction losses Q_{gas}^{-1}, surface losses Q_{surface}^{-1}, and thermoelastic dissipation Q_{TED}^{-1}. In this work we particularly focus on thermoelastic dissipation contribution Q_{TED}^{-1}, where the vibration disrupts the equilibrium of the oscillator, and the strain field induced by vibration couples with the temperature field, leading to energy dissipation. So total dissipation combines thermoelastic and other dissipative mechanisms:

$$Q^{-1} = Q_{\text{TED}}^{-1} + Q_{\text{other}}^{-1}. \tag{2}$$

In a 2D NEMS resonator, the energy is composed of three distinct components: W_{flex}, generated by membrane flexing; W_{elong}, generated by membrane elongation; and W_{tensile}, the tensile energy:

$$\begin{cases} W_{\text{elong}} = \dfrac{1}{8}\displaystyle\int_0^w S dy \int_0^L E\left(\frac{\partial u}{\partial x}\right)^4 dx, \\ W_{\text{flex}} = \dfrac{1}{2}\displaystyle\int_0^w dy \int_0^L EI_z\left(\frac{\partial^2 u}{\partial x^2}\right)^2 dx, \\ W_{\text{tensile}} = \dfrac{1}{2}\varepsilon E\displaystyle\int_0^w S dy \int_0^L \left(\frac{\partial u}{\partial x}\right)^2 dx, \end{cases} \tag{3}$$

where I_z, E, L and S represent the moment of inertia, Young's modulus, length and cross-sectional area of the suspended strip, respectively. ε is the total axial tensile strain dependent on V_G and $u = \delta z_m \sin(n\pi x/L)$ is the sinus-type shape of the doubly-clamped resonator, where n and δz_m are the modal number and the maximum vibration amplitudes of the suspended strip, respectively. We further substitute the mode shapes into the above equation and get

$$\begin{cases} W_{\text{elong}} = \dfrac{3}{64}\dfrac{ES(n\pi\delta z)^4}{L^3}, \\ W_{\text{flex}} = \dfrac{1}{48}\dfrac{ES(t\delta z)^2(n\pi)^4}{L^3}, \\ W_{\text{tensile}} = \dfrac{1}{4}\dfrac{\varepsilon ES(n\pi\delta z)^2}{L}. \end{cases} \tag{4}$$

The dissipation caused by flexing and elongation constitutes thermoelastic dissipation, and the expression of thermoelastic dissipation is obtained:

$$\begin{aligned} Q_{\text{TED}}^{-1} &= \frac{\Delta W_{\text{elong}} + \Delta W_{\text{flex}}}{2\pi\left(W_{\text{tensile}} + W_{\text{elong}} + W_{\text{flex}}\right)} \\ &\approx \underbrace{\frac{W_{\text{elong}}}{W_{\text{tensile}}}\frac{\Delta W_{\text{elong}}}{2\pi W_{\text{elong}}}}_{Q_{\text{elong}}^{-1}} + \underbrace{\frac{W_{\text{flex}}}{W_{\text{tensile}}}\frac{\Delta W_{\text{flex}}}{2\pi W_{\text{flex}}}}_{Q_{\text{flex}}^{-1}}, \end{aligned} \tag{5}$$

where ΔW_{elong} and ΔW_{flex} are the loss of elongation and flexing energy during a cycle, respectively.

The response of an inelastic material to a constant stress happens at a certain relaxation time; i.e., the induced strain lags the stress by one phase, which leads to energy dissipation. We often use the loss angle to calculate the energy dissipation in our system. This loss angle is related to the complex form of the Young's modulus of the material: $E^* = E + E' = E(1 + i\delta)$, where E represents the real part of Young's modulus which defines the amount of energy stored in the specimen as a result of the applied strain, E' is the lost Young's modulus and represents the dissipation of energy, and δ represents the loss angle [44]. In a 2D membrane, the loss angles due to elongation and flexing losses are $\delta_{\text{elong}} = \Delta W_{\text{elong}}/(2\pi W_{\text{elong}})$ and $\delta_{\text{flex}} = \Delta W_{\text{flex}}/(2\pi W_{\text{flex}})$, respectively. It can be confidently assumed that δ_{elong} and δ_{flex} remain constant in the MoS_2 device as V_G or δV_G changes. Then we can get the thermoelastic dissipation expressions, including elongation dissipation and flexing dissipation:

$$Q_{\text{TED}}^{-1} = \underbrace{\frac{3(n\pi)^2}{16\varepsilon}\left(\frac{\delta z}{L}\right)^2 \delta_{\text{elong}}}_{Q_{\text{elong}}^{-1}} + \underbrace{\frac{(n\pi)^2}{12\varepsilon}\left(\frac{t}{L}\right)^2 \delta_{\text{flex}}}_{Q_{\text{flex}}^{-1}}. \tag{6}$$

The derived equation reveals a fundamental competition between static tensile strain ε and dynamic vibration amplitude δz in governing thermoelastic dissipation Q_{TED}^{-1} of electrostatically gated 2D NEMS resonators. Specifically, Q_{TED}^{-1} decreases with ε and increases with δz, this dual dependence aligns with the previous analysis. At elevated gate voltages V_G, electrostatic forces induce tensile elongation of the resonator, increasing ε and stored mechanical energy ($W_{\text{tensile}} \propto \varepsilon$), thereby suppressing dissipation and enhancing Q. Concurrently, higher V_G amplifies the driving force, enlarging δz and intensifying thermoelastic losses ($W_{\text{elong}} \propto (\delta z)^4$), which reduces Q. The net Q-V_G dependence is dictated by the dominance of these antagonistic factors. When ε modulation outweighs δz effects ($(\frac{\partial \varepsilon}{\partial V_G}) \gg (\frac{\partial \delta z}{\partial V_G})$), Q increases with V_G; conversely, in amplitude-dominated regimes ($(\frac{\partial \delta z}{\partial V_G}) \gg (\frac{\partial \varepsilon}{\partial V_G})$), Q decreases despite rising V_G. Quantitative analysis of this strain-to-amplitude sensitivity ratio establishes critical thresholds for polarity reversal, resolving prior inconsistencies in literature.

The process described in the provided discussion involves the definition of the initial strain ε_0 through fitting the resonant frequency tuning curve and then determining the total strain ε due to V_G. At electrostatic stretching equilibrium, where the elastic and electrostatic forces are balanced and the static displacement z_e of the strip can be determined by minimizing the total energy (elastic and electrostatic) $\frac{\partial (U_{\text{es}} - U_{\text{el}})}{\partial z} = 0$. One can define the offset function of the whole strip $Z = 4z\left(Lx - x^2\right)/L^2$. Subsequently, the total strain induced by the elongation caused by V_G can be calculated $\varepsilon = \frac{1+\varepsilon_0}{L}\int_0^L \sqrt{1 + (\frac{\partial Z}{\partial x})^2}dx - 1$ (see Appendix B.1 for details). By utilizing this method based on the resonant frequency tuning curve, the initial strain and tensile strain at different DC voltages can be extracted. The variation of total strain with DC voltage can be depicted in Figure 1(e), providing insights into how strain changes with varying DC voltage levels.

To solve for the vibration amplitude δz, the 2D resonator is treated as a linear resonator vibrating at its equilibrium, and it is only subjected to a driving force $F(t)$. The equation of motion is represented by $\ddot{x} + \frac{\gamma}{m_{\text{eff}}}\dot{x} + \omega_0^2 x = \frac{F(t)}{m_{\text{eff}}}$, where x is the transient displacement in the out-of-plane direction, ω_0 is the angular resonance frequency, $F(t) = F_{\text{drive}}\cos(\omega t)$ represents the transient external RF driving force, and γ stands for the linear damping factor. Solving the equation results in the classical linear vibration amplitude x_0:

$$|x_0(\omega)|^2 = \frac{\left(\frac{F_{\text{drive}}}{m_{\text{eff}}}\right)^2}{\left(\omega^2 - {\omega_0}^2\right)^2 + (\gamma\omega)^2}, \tag{7}$$

where F_{drive} is the electrostatic drive, m_{eff} is the equivalent mass, which in a 2D strip resonator is equal to half the actual mass. When the resonator is at the resonant frequency $\omega = \omega_0$, the expression for δz is obtained as $\delta z = \frac{F_{\text{drive}}}{m_{\text{eff}} \cdot \gamma \cdot \omega_0}$. In our calculations it is considered that the vibration amplitude is directly proportional to the DC and AC voltages, given by $\delta z = b \cdot |\delta V_G \cdot V_G|$, with the vibration amplitude coefficient b depending on the dimensions of the resonator and gap g (refer to Appendix B.3 for specifics). After evaluating the coefficient as $b = 3.7 \times 10^{-9}$ and fixed $\delta V_G = 2.5$ mV, the variation of vibration amplitude with V_G is depicted in Figure 1(f).

As V_G is raised from 0 to 40 V, δz increases from 0 to 0.377 nm, with the total strain being increased only by 2×10^{-6}. This indicates that the vibration amplitude δz responds more rapidly to changes in V_G compared to strain ε, highlighting its greater impact on Q. The final Q is observed to decrease with V_G's increment. Figure 1(i) illustrates the reduction of Q as V_G increases, as determined from our experiments. The Q are derived by fitting the resonance curve (Figures 1(g) and (h)) (refer to Appendix C.3 for specifics). By varying V_G from -0.8 to -40.0 V,

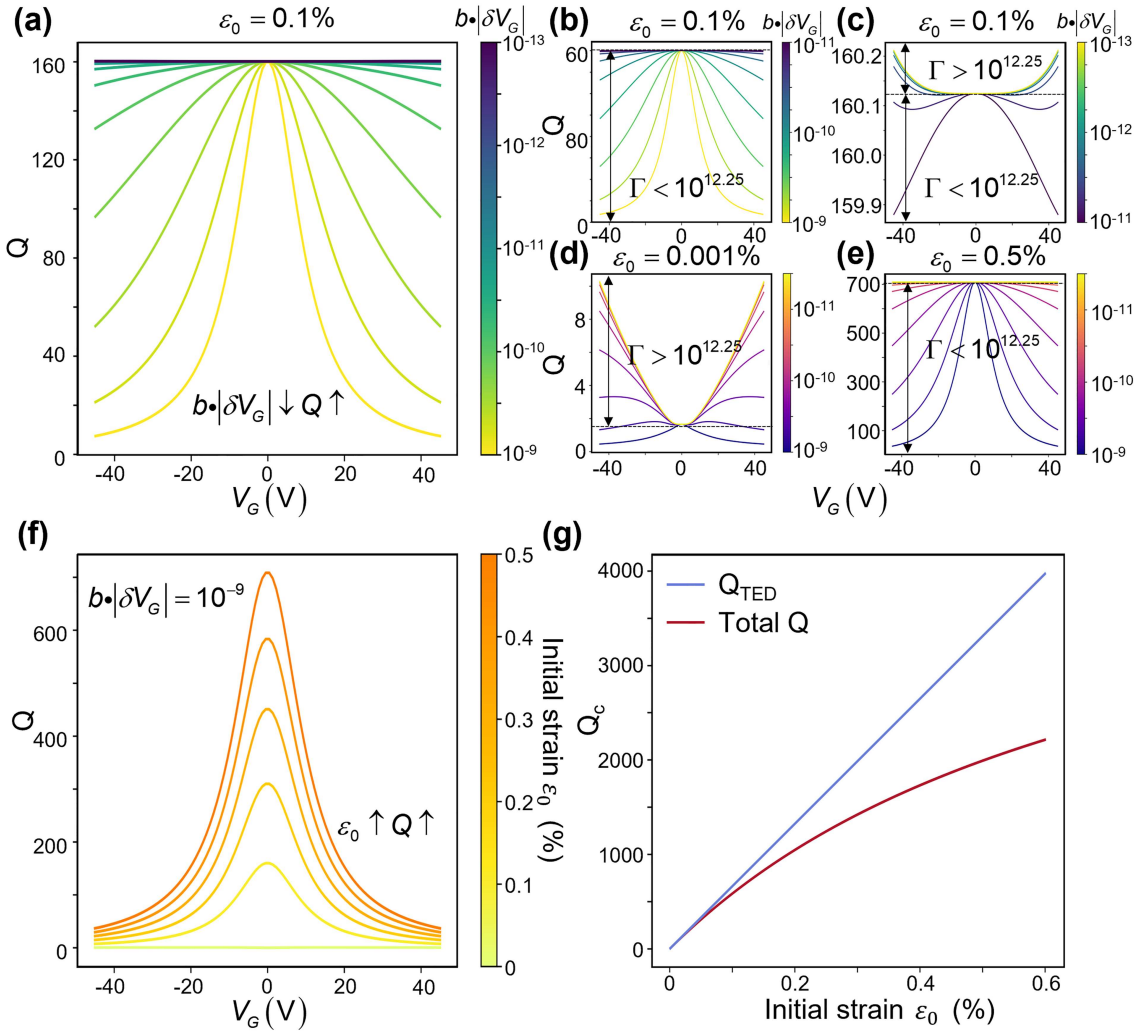

Figure 2 (Color online) Theoretical simulation of the effect of vibration amplitude and initial strain on variation of Q with DC voltage. (a) The variation of Q with V_G by varying the product of the vibration amplitude coefficient and the AC driving voltage $b \cdot |\delta V_G|$ from 10^{-9} to 10^{-13} for a fixed initial strain of 0.1% and the loss angles due to elongation and flexing losses being $\delta_{\text{elong}} = 0.06$ and $\delta_{\text{flex}} = 0.04$, respectively. The details are shown in (b) and (c). (d) and (e) Dependence of Q on V_G fixes the initial strain at 0.001% and 0.5%, respectively, where Γ is the strain-to-amplitude sensitivity ratio $\Gamma = (\partial\varepsilon/\partial V_G)/(\partial\delta z/\partial V_G)$. (f) Fixed $b \cdot |\delta V_G| = 10^{-9}$, and adjusted the initial strain from 0 to 0.5%, which shows that the trend of Q with V_G remains unchanged, and Q is taken to be maximum when $V_G = 0$. (g) Dependence of the critical value of Q_{TED} and total Q on the initial strain ε_0 at $V_G = 0$.

Q decreases from 2138 to 208, and obtains $\Delta Q/Q = 928\%$, aligning with theoretical analysis to maintain resonance data in the linear state. Non-linear state data have been excluded to ensure all measurements are linear.

However, the trend of Q-factor dependence for the MoS_2 strip resonator in this study appears opposite to that in [48]. To investigate this discrepancy, we conducted theoretical simulations to analyze the impact of vibration amplitude and strain on Q. Our findings indicate that the main reason for this contrasting trend is the difference in strain and amplitude with DC voltage for different resonators. We can define the strain-to-amplitude sensitivity ratio $\Gamma = \left(\frac{\partial\varepsilon}{\partial V_G}\right) / \left(\frac{\partial\delta z}{\partial V_G}\right)$, which determines the polarity of the Q-V_G relationship. From the previous analysis, we can calculate $\frac{\partial\delta z}{\partial V_G} = b \cdot |\delta V_G|$, and $\frac{\partial\varepsilon}{\partial V_G} \approx 1/\varepsilon_0$. By examining the data from the MoS_2 resonator in Figure 1, while keeping elongation and flexural energy parameters constant, we focused on the effects of initial strain and the product of vibration amplitude coefficients and AC driving voltage $b \cdot |\delta V_G|$ on Q. In Figure 2(a), with fixed initial strain at 0.1%, varying $b \cdot |\delta V_G|$ revealed that for large $b \cdot |\delta V_G|$ (representing large vibration amplitude), the vibration amplitude had a significant impact on Q, leading to a decrease with increasing V_G; as $b \cdot |\delta V_G|$ decreased, the influence of vibration amplitude on Q reduced, resulting in a gradual slowdown in Q decrease until the effects of vibration amplitude and strain (unit in %) on Q were nearly balanced ($\Gamma \approx 1/\varepsilon_0 \cdot (b \cdot |\delta V_G|) = 10^{12.25}$), maintaining Q relatively constant as V_G increased; with further decrease in $b \cdot |\delta V_G|$, strain's effect on Q became more prominent ($\Gamma \approx 1/\varepsilon_0 \cdot (b \cdot |\delta V_G|) > 10^{12.25}$), causing Q to rise with increasing V_G, which has been experimentally validated [48].

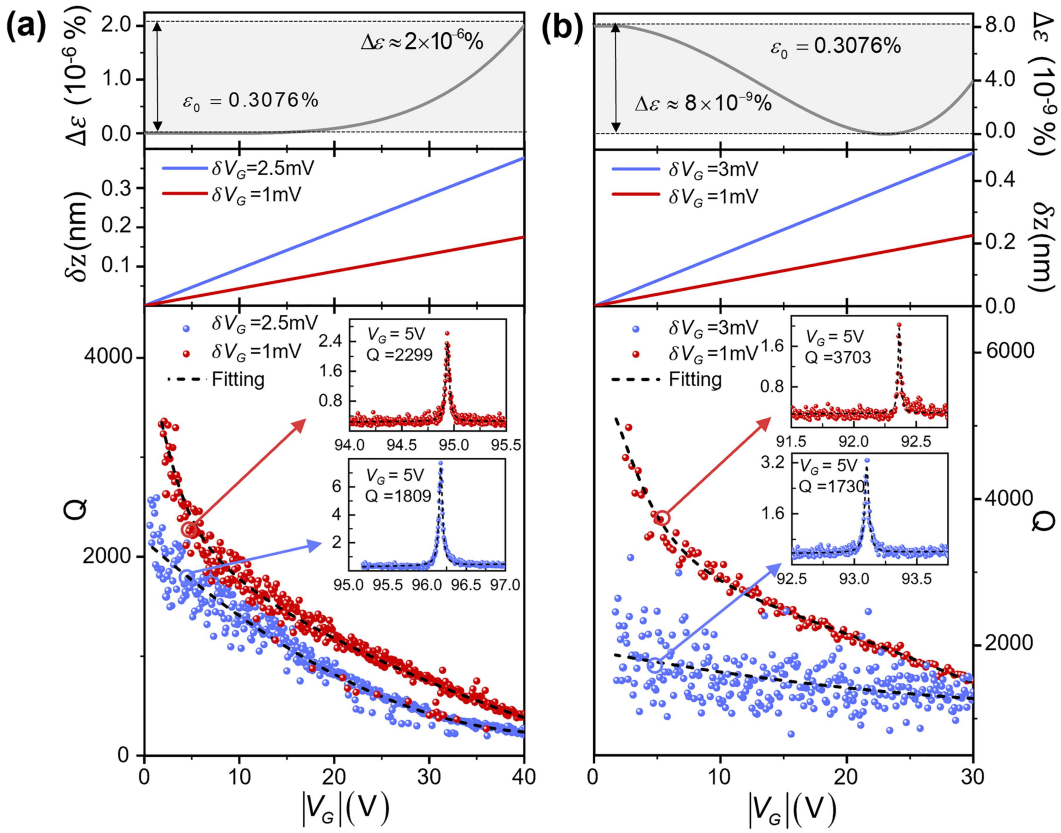

Figure 3 (Color online) Dependence of Q on static DC strain at two different AC driving voltages δV_G for a doubly-clamped MoS_2 resonator. (a) For the doubly-clamped MoS_2 in Figure 1, V_G is scanned from 0 to 40 V to obtain the variation of strain ε with V_G, the strain is varied by the amount of strain $\Delta\varepsilon = 2 \times 10^{-6}$, the δV_G are fixed to 2.5 mV (blue) and 1 mV (red), respectively, δz is plotted as a function of V_G firstly, and then Q is plotted as a function of V_G, with the scattered dots displaying the measured data, and dashed lines displaying the fitted curves using our model. The small plot in the upper right corner plots the resonance spectra measured at different δV_G. V_G is fixed at 5 V, and Q decreases from 2299 to 1809 when δV_G is increased from 1 to 2.5 mV. (b) For another doubly-clamped MoS_2 with length $L = 1.3$ μm, width $w = 1.9$ μm, and thickness $t = 49$ nm, the V_G is scanned from 0 to 30 V, and the δV_G are fixed at 1 mV (red) and 3 mV (blue), respectively. The ε and δz are obtained, and the curves of Q versus V_G are plotted. V_G is fixed at 5 V, and Q decreased from 3703 to 1730 when δV_G is increased from 1 to 3 mV.

Similar trends were observed when varying $b \cdot |\delta V_G|$ while fixing the initial strain at 0.001% (Figure 2(d)) and 0.5% (Figure 2(e)), respectively.

Upon fixing $b \cdot |\delta V_G|$ and varying the initial strain ε_0, Q decreases with V_G, with the rate of decrease influenced by the initial strain; higher initial strains exhibit a faster decline (Figure 2(f)). Furthermore, when $V_G = 0$, the total strain equals the initial strain $\varepsilon = \varepsilon_0$, and $\delta z = 0$. By substituting these values into the thermoelastic dissipation formula, the critical dissipation value is obtained:

$$Q_{\mathrm{TED,c}}^{-1} = \frac{(n\pi)^2}{12\varepsilon_0}\left(\frac{t}{L}\right)^2 \delta_{\mathrm{flex}}. \tag{8}$$

At this juncture, thermoelastic dissipation is solely linked to the initial strain, with $Q_{\mathrm{TED,c}}$ and total Q_c increasing as the initial strain rises, as illustrated in Figure 2(g). This behavior is attributed to the higher storage of potential energy within the resonator at elevated initial strains.

To validate this finding, the quality factor (Q) of the 2D NEMS resonator was assessed at varying AC driving voltages. Increasing the δV_G applied to the MoS_2 resonator in Figure 1 to 2.5 mV, while maintaining other parameters constant, and raising V_G from 0 to 40 V, allowed for Q determination through spectral fitting (Figure 3(a)). When δV_G is increased from 1 to 2.5 mV at a constant DC voltage, Q decreases due to amplified vibration amplitude leading to increased elongation dissipation. Despite the rise in δV_G, the combined effect of increased vibration amplitude is insufficient to counterbalance the strain growth ($\Gamma < 10^{12.25}$), leading to a continued decline in Q. An additional test has been performed with another doubly-clamped MoS_2 resonator (Figure 3(b)) length $L = 1.3$ μm, width $w = 1.9$ μm, and thickness $t = 49$ nm. δV_G set at 1 and 3 mV, respectively, and V_G scanned from 0 to 30 V, revealed the significant decrease in Q when $\delta V_G = 3$ mV, showing consistency with the simulation results presented

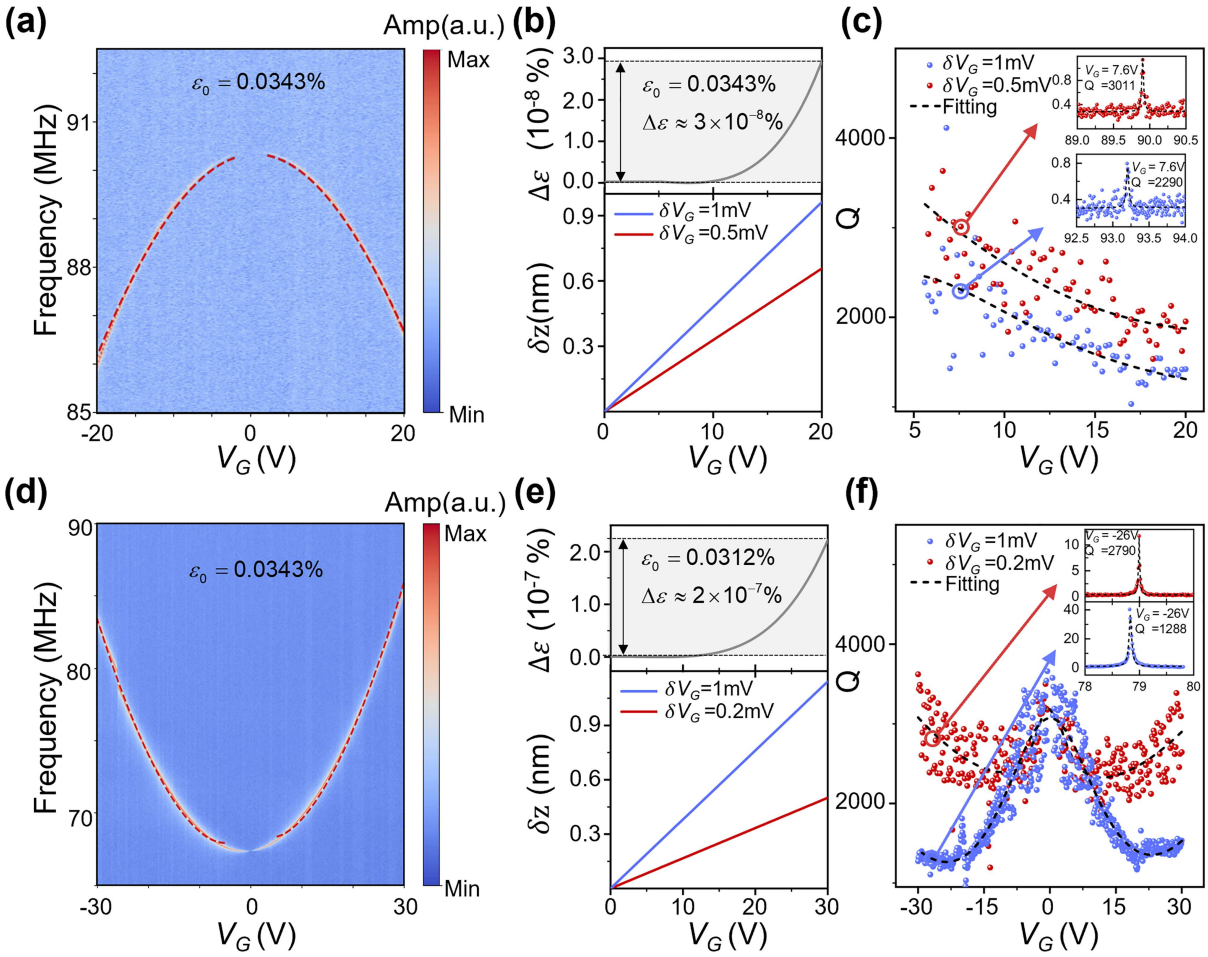

Figure 4 (Color online) Dependence of Q on AC driving voltage δV_G for doubly-clamped graphene resonators. (a)–(c) The dependence of ε and δz, as well as Q on the δV_G, was conducted for sample#1 doubly-clamped graphene resonator with length $L = 2.8$ μm, width $w = 1.4$ μm, and thickness $t = 14$ nm. (a) The V_G was scanned from −20 to 20 V, with δV_G fixed at 1 mV. The resonance spectra were then measured for different V_G and an initial strain $\varepsilon_0 = 0.0343\%$ was extracted. The signal amplitude is color-coded, and the red dashed line indicates the fit of the resonance frequency tuning. (b) Variation of strain with V_G for a strain variation of $\Delta\varepsilon = 3 \times 10^{-8}\%$. The vibration amplitude is plotted as a function of V_G by fixing the δV_G to 1 mV (blue) and 0.5 mV (red), respectively. (c) The curve of Q as a function of V_G, with the scatter showing the measured data and the dashed line showing the fitted curve using our model. The small plot in the upper right corner depicts the resonance spectra measured at different δV_G, with V_G fixed at 7.5 V, and Q decreasing from 3011 to 2290 as δV_G is increased from 0.5 to 1 mV. (d)–(f) The dependence of strain and vibration amplitude, as well as Q on the δV_G, was conducted for sample#2 doubly-clamped graphene resonator with length $L = 2.8$ μm, width $w = 1.2$ μm, and thickness $t = 17$ nm. (d) The V_G was scanned from −30 to 30 V, with the δV_G fixed at 1 mV. The resonance spectra were then measured at different V_G, from which the initial strain $\varepsilon_0 = 0.0312\%$ was extracted. (e) The δV_G was fixed at 1 mV (blue) and 0.2 mV (red), respectively. ε and δz with V_G are plotted. (f) The curve of Q with V_G. V_G was fixed at −26 V, and Q decreased from 2790 to 1288 as δV_G increased from 0.2 to 1 mV.

in Figure 2.

To validate the universal scalability of our model, we systematically characterized multiple doubly-clamped graphene resonators under controlled electrostatic conditions. For Sample #1, with the AC drive voltage fixed at $\delta V_G = 1$ and 0.5 mV, the amplitude-mediated dissipation dominated over strain effects ($\Gamma < 10^{12.25}$), resulting in a consistent Q reduction as δV_G increased (Figure 4(c)). This trend persisted across the full V_G sweep range ($0 < V_G < 20$ V), confirming the prevalence of nonlinear phonon coupling in high-drive regimes. Sample #2 further demonstrated the critical role of drive amplitude in dissipation polarity. At $\delta V_G = 1$ mV, amplitude dominance ($\Gamma < 10^{12.25}$) again led to a decrease in Q as V_G increased, whereas reducing δV_G to 0.2 mV shifted the system to a strain-dominated regime ($\Gamma > 10^{12.25}$), where Q increased with V_G (Figure 4(f)). This reversible polarity switching, achieved solely by modulating δV_G, underscores the universality of our strain-amplitude sensitivity criterion across 2D material systems. The non-monotonic behavior of the Q factor as a function of gate voltage enables electrical reconfiguration of the resonator's performance: a single device can be tuned between a high-Q state (for high sensitivity and narrowband operation) and a low-Q state (for fast response and wideband operation).

Research indicates that thermoelastic damping depends not only on mechanical resonance frequency and geo-

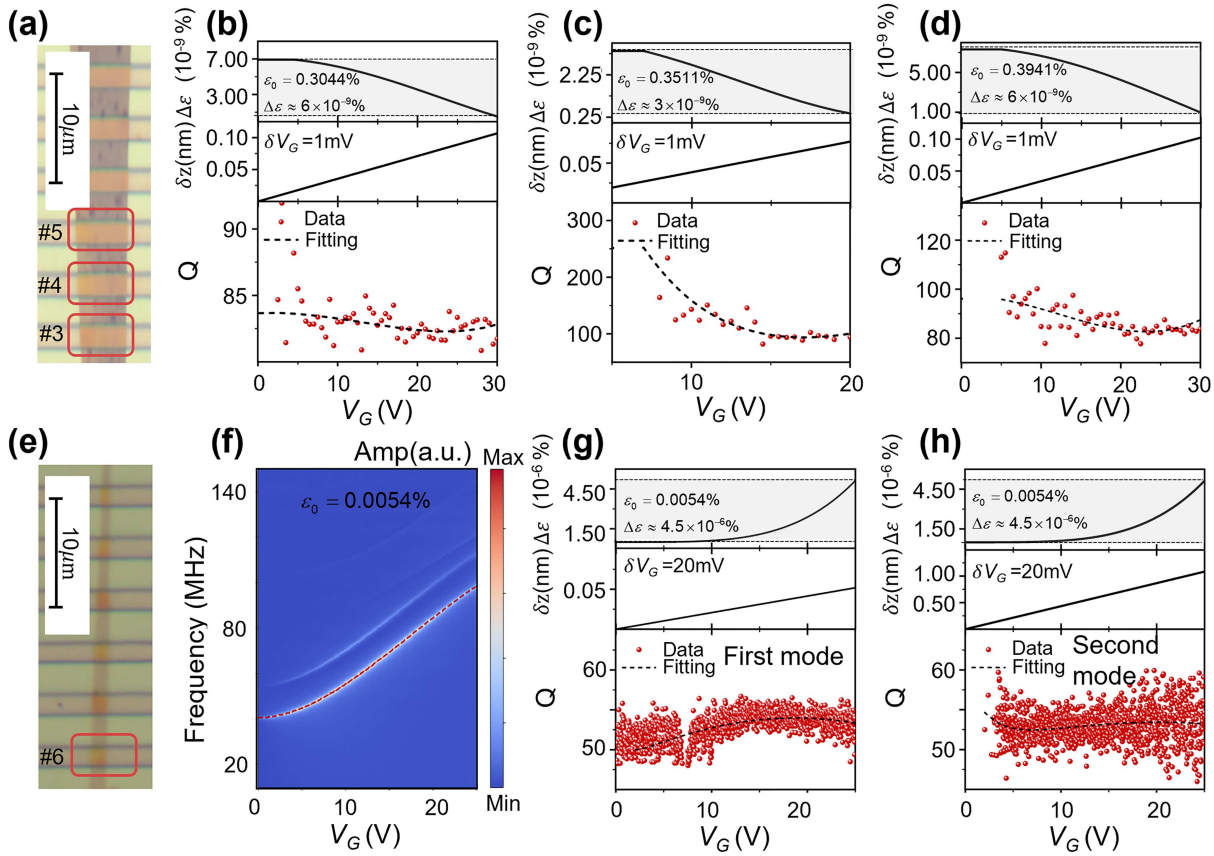

Figure 5 (Color online) Dependence of Q on AC driving voltage δV_G for doubly-clamped graphene resonators at room temperature. (a) Optical image of sample#3 with length $L = 2$ μm, width $w = 4.3$ μm, and thickness $t = 16$ nm, sample#4 with length $L = 2$ μm, width $w = 4.5$ μm, and thickness $t = 16$ nm, and sample#5 with length $L = 2$ μm, width $w = 4.7$ μm, and thickness $t = 16$ nm (serially connected double-clamped graphene resonators); (b)–(d) The dependence of ε and δz, as well as Q on the δV_G, was conducted for sample#3, sample#4 and sample#5, respectively. (e) Optical image of sample #6 with length $L = 2$ μm, width $w = 1.5$ μm, and thickness $t = 14$ nm. (f) The V_G was scanned from 0 to 25 V, with δV_G fixed at 20 mV. The resonance spectra were then measured for different V_G. An initial strain $\varepsilon_0 = 0.0054\%$ was extracted. The signal amplitude is color-coded, and the red dashed line indicates the fit of the resonance frequency tuning. (g) and (h) The dependence of ε and δz, as well as Q on the δV_G, was conducted for the first and second modes of sample#6, respectively. All samples were tested at room temperature.

metric shape, but also significantly on operating temperature [49]. Therefore, we also conducted Q tests at room temperature, as shown in Figure 5. Experimental verification confirms that although the value of Q is affected by increased thermal dissipation, the strain-amplitude antagonism mechanism remains effective at room temperature. Simultaneously, we used (8) to fit the first and second modes of a doubly-clamped graphene strip (Figures 5(e)–(h)). While our primary focus is on the first mode, experiments demonstrate that our theory is equally applicable to the second mode.

Complementary measurements were performed on additional doubly-clamped MoS_2 and graphene NEMS resonators with varied geometries and material parameters. Devices exhibiting pronounced vibration amplitude dependence on DC voltage ($\frac{\partial \delta z}{\partial V_G} \gg \frac{\partial \varepsilon}{\partial V_G}$) demonstrated a consistent $Q \propto 1/V_G$ trend, whereas those dominated by strain modulation ($\frac{\partial \varepsilon}{\partial V_G} \gg \frac{\partial \delta z}{\partial V_G}$) showed $Q \propto V_G$ enhancement (refer to Appendix D.3). Systematic analysis revealed that increasing the AC driving voltage δV_G to amplify vibration amplitude resulted in higher dissipation and thermoelastic damping due to enhanced coupling to phonons, leading to a decrease in Q with increasing δV_G. These findings offer valuable insights for optimizing Q in 2D NEMS resonators, suggesting that higher Q can be achieved by applying large tensile strains and small drive amplitudes, adjusting the initial strain, reducing the vibration amplitude coefficient b, and lowering δV_G. Furthermore, the decrease in loss angles δ_{elong} and δ_{flex} with temperature contributes to higher Q at lower temperatures, consistent with prior research [39, 50, 51]. Lastly, our theory aligns with the dissipative dilution theory [46], providing the method to manipulate Q by adjusting initial strain and oscillation amplitude to influence the dissipative dilution factor D (refer to Appendix C.2).

4 Conclusion

In conclusion, this study establishes a dual-parameter engineering framework that resolves the long-standing challenge of deterministic dissipation control in 2D NEMS resonators. Through coupled theoretical modeling and experimental validation across doubly-clamped MoS_2 and graphene resonators, we demonstrate that the quality factor (Q) is governed by the antagonistic interplay between static tensile strain (ε) and dynamic vibration amplitude (δz).

Increasing the DC gate voltage V_G simultaneously enhances ε through static deflection, which suppresses dissipation, while a larger V_G also amplifies the driving force, leading to an increase in δz and an increase in dissipation. Crucially, we identify a critical strain-to-amplitude sensitivity ratio $(\partial\varepsilon/\partial V_G)/(\partial\delta z/\partial V_G)$ that dictates the polarity of the Q-V_G relationship. When the initial stress of the oscillator is large, the enhancement of the tensile strain by V_G diminishes, in contrast to amplifying the enhancement of the dissipation by δz, which leads to a decrease in Q with increasing V_G. By strategically balancing these competing effects, we achieve programmable Q modulation, including non-monotonic transitions and a record-breaking tunability range $\Delta Q/Q = 928\%$. This capability for dynamic performance reconfiguration—tuning between high sensitivity and rapid response—is particularly valuable for next-generation adaptive sensing, communication systems, and on-chip signal processing, where operational requirements can vary dynamically. This work, therefore, provides a versatile and powerful strategy for the tailored optimization of 2D NEMS resonators, advancing their application in technologies requiring precision dissipation management.

Acknowledgements This work was supported by National Key Research and Development Program of China (Grant No. 2022YFA1405900), National Natural Science Foundation of China (Grant Nos. 12074058, 92565107), Innovation Program for Quantum Science and Technology (Grants No. 2021ZD0302300), and Sichuan Science and Technology Program (Grant Nos. 2024YFHZ0372, 2024ZYD0156). We extend our gratitude to Sichuan Jiuzhou Electric Group Co., Ltd. and the HSE University Centre for Basic Science Research for their support.

Supporting information Appendixes A–D. The supporting information is available online at info.scichina.com and link.springer.com. The supporting materials are published as submitted, without typesetting or editing. The responsibility for scientific accuracy and content remains entirely with the authors.

References

1 Roukes M. Nanoelectromechanical systems face the future. Phys World, 2001, 14: 25–32
2 Craighead H G. Nanoelectromechanical Systems. Science, 2000, 290: 1532–1535
3 Yang Y T, Ekinci K L, Huang X M H, et al. Monocrystalline silicon carbide nanoelectromechanical systems. Appl Phys Lett, 2001, 78: 162–164
4 Jensen K, Peng H B, Zettl A. Limits of nanomechanical resonators. In: Proceedings of International Conference on Nanoscience and Nanotechnology, Brisbane, 2006. 4143332
5 Rugar D, Budakian R, Mamin H J, et al. Single spin detection by magnetic resonance force microscopy. Nature, 2004, 430: 329–332
6 Jensen K, Kim K, Zettl A. An atomic-resolution nanomechanical mass sensor. Nat Nanotech, 2008, 3: 533–537
7 Chiu H Y, Hung P, Postma H W C, et al. Atomic-scale mass sensing using carbon nanotube resonators. Nano Lett, 2008, 8: 4342–4346
8 Chaste J, Eichler A, Moser J, et al. A nanomechanical mass sensor with yoctogram resolution. Nat Nanotech, 2012, 7: 301–304
9 Massel F, Heikkilä T T, Pirkkalainen J M, et al. Microwave amplification with nanomechanical resonators. Nature, 2011, 480: 351–354
10 Hertzberg J B, Rocheleau T, Ndukum T, et al. Back-action-evading measurements of nanomechanical motion. Nat Phys, 2010, 6: 213–217
11 Teufel J D, Donner T, Castellanos-Beltran M A, et al. Nanomechanical motion measured with an imprecision below that at the standard quantum limit. Nat Nanotech, 2009, 4: 820–823
12 O'Connell A D, Hofheinz M, Ansmann M, et al. Quantum ground state and single-phonon control of a mechanical resonator. Nature, 2010, 464: 697–703
13 Zhang H. Ultrathin two-dimensional nanomaterials. ACS Nano, 2015, 9: 9451–9469
14 Qiu H, Yu Z H, Zhao T G, et al. Two-dimensional materials for future information technology: status and prospects. Sci China Inf Sci, 2024, 67: 160400
15 Lemes M F S, Pimenta A C S, Lozano Calderón G, et al. Polarization-dependent plasmon-induced doping and strain effects in MoS_2 monolayers on gold nanostructures. ACS Nano, 2025, 19: 2518–2528
16 Tian F, Wu S X, Liu X Y, et al. High quantum efficiency ultraviolet photodetector based on graphene and truncated silicon nanocones. Sci China Inf Sci, 2025, 68: 140405
17 Liu Y, Huang Y, Duan X. Van der Waals integration before and beyond two-dimensional materials. Nature, 2019, 567: 323–333
18 Saito Y, Nojima T, Iwasa Y. Highly crystalline 2D superconductors. Nat Rev Mater, 2016, 2: 1–8
19 Schaibley J R, Yu H, Clark G, et al. Valleytronics in 2D materials. Nat Rev Mater, 2016, 1: 1–5
20 von Klitzing K, Chakraborty T, Kim P, et al. 40 years of the quantum Hall effect. Nat Rev Phys, 2020, 2: 397–401
21 Kang H, Ma J, Li J, et al. Exciton polaritons in emergent two-dimensional semiconductors. ACS Nano, 2023, 17: 24449–24467
22 Massicotte M, Vialla F, Schmidt P, et al. Dissociation of two-dimensional excitons in monolayer WSe_2. Nat Commun, 2018, 9: 1633
23 Feng P X-L. Resonant nanoelectromechanical systems (NEMS): progress and emerging frontiers. In: Proceedings of IEEE 33rd International Conference on Micro Electro Mechanical Systems (MEMS), Vancouver, 2020. 212–217
24 Xu B, Zhang P, Zhu J, et al. Nanomechanical resonators: toward atomic scale. ACS Nano, 2022, 16: 15545–15585
25 Bunch J S, van der Zande A M, Verbridge S S, et al. Electromechanical resonators from graphene sheets. Science, 2007, 315: 490–493
26 Ferrari P F, Kim S P, van der Zande A M. Nanoelectromechanical systems from two-dimensional materials. Appl Phys Rev, 2023, 10: 031302
27 Lee J, Wang Z, He K, et al. High frequency MoS_2 nanomechanical resonators. ACS Nano, 2013, 7: 6086–6091
28 Cassella C, Piazza G. AlN two-dimensional-mode resonators for ultra-high frequency applications. IEEE Electron Device Lett, 2015, 36: 1192–1194
29 Sage E, Sansa M, Fostner S, et al. Single-particle mass spectrometry with arrays of frequency-addressed nanomechanical resonators. Nat Commun, 2018, 9: 3283
30 Wei C, Zhang Y. The ultra-high sensitivity of mass resonator achieved by the beam with variable thickness. Results Phys, 2023, 49: 106483

31 Dominguez-Medina S, Fostner S, Defoort M, et al. Neutral mass spectrometry of virus capsids above 100 megadaltons with nanomechanical resonators. Science, 2018, 362: 918–922
32 Lee J, Wang Z, He K, et al. Electrically tunable single- and few-layer MoS_2 nanoelectromechanical systems with broad dynamic range. Sci Adv, 2018, 4: 6653
33 Miller J M L, Ansari A, Heinz D B, et al. Effective quality factor tuning mechanisms in micromechanical resonators. Appl Phys Rev, 2018, 5: 041307
34 Gabrielson T B. Mechanical-thermal noise in micromachined acoustic and vibration sensors. IEEE Trans Electron Devices, 1993, 40: 903–909
35 Gabrielson T B. Fundamental noise limits for miniature acoustic and vibration sensors. J Vib Acoustics, 1995, 117: 405–410
36 Altug H, Oh S H, Maier S A, et al. Advances and applications of nanophotonic biosensors. Nat Nanotechnol, 2022, 17: 5–16
37 Gregory J A, Cho J, Najafi K. Characterization and control of a high-Q MEMS inertial sensor using low-cost hardware. In: Proceedings of the 2012 IEEE/ION Position, Location and Navigation Symposium, Myrtle Beach, 2012. 239–247
38 Guo R, He Q, Zhang Z, et al. High-Q silicon microring resonator with ultrathin sub-wavelength thicknesses for sensitive gas sensing. Appl Phys Rev, 2024, 11: 021417
39 Chen C, Rosenblatt S, Bolotin K I, et al. Performance of monolayer graphene nanomechanical resonators with electrical readout. Nat Nanotech, 2009, 4: 861–867
40 Koskenvuori M, Tittonen I. GHz-range FSK-reception with microelectromechanical resonators. Sens Actuat A-Phys, 2008, 142: 346–351
41 Nabki F, Allidina K, Ahmad F, et al. A highly integrated 1.8 GHz frequency synthesizer based on a MEMS resonator. IEEE J Solid-State Circuits, 2009, 44: 2154–2168
42 Lee J, Shaw S W, Feng P X L. Giant parametric amplification and spectral narrowing in atomically thin MoS_2 nanomechanical resonators. Appl Phys Rev, 2022, 9: 011404
43 Zheng L, Zhang J, Wang H, et al. RF NEMS switches based on graphene for low pull-in voltage and excellent RF performance. Sci Rep, 2024, 14: 23346
44 Schmid S, Villanueva L G, Roukes M L. Fundamentals of Nanomechanical Resonators. Cham: Springer International Publishing, 2023
45 Naeem A, Rehmani M H, Saleem Y, et al. Network coding in cognitive radio networks: a comprehensive survey. IEEE Commun Surv Tut, 2017, 19: 1945–1973
46 Engelsen N J, Beccari A, Kippenberg T J. Ultrahigh-quality-factor micro- and nanomechanical resonators using dissipation dilution. Nat Nanotechnol, 2024, 19: 725–737
47 Verbridge S S, Shapiro D F, Craighead H G, et al. Macroscopic tuning of nanomechanics: substrate bending for reversible control of frequency and quality factor of nanostring resonators. Nano Lett, 2007, 7: 1728–1735
48 Zhang P, Jia Y, Xie M, et al. Strain-modulated dissipation in two-dimensional molybdenum disulfide nanoelectromechanical resonators. ACS Nano, 2022, 16: 2261–2270
49 Wu G, Xu J, Ng E J, et al. MEMS resonators for frequency reference and timing applications. J Microelectromech Syst, 2020, 29: 1137–1166
50 Eichler A, Moser J, Chaste J, et al. Nonlinear damping in mechanical resonators made from carbon nanotubes and graphene. Nat Nanotech, 2011, 6: 339–342
51 Güttinger J, Noury A, Weber P, et al. Energy-dependent path of dissipation in nanomechanical resonators. Nature Nanotech, 2017, 12: 631–636